ACS APPLIED MATERIALS & INTERFACES

www.acsami.org

Research Article

3D Printing Latex: A Route to Complex Geometries of High Molecular Weight Polymers

Philip J. Scott,[#] Viswanath Meenakshisundaram,[#] Maruti Hegde, Christopher R. Kasprzak, Christopher R. Winkler, Keyton D. Feller, Christopher B. Williams, and Timothy E. Long*

Cite This: *ACS Appl. Mater. Interfaces* 2020, 12, 10918−10928

Read Online

ACCESS | Metrics & More | Article Recommendations | Supporting Information

ABSTRACT: Vat photopolymerization (VP) additive manufacturing fabricates intricate geometries with excellent resolution; however, high molecular weight polymers are not amenable to VP due to concomitant high solution and melt viscosities. Thus, a challenging paradox arises between printability and mechanical performance. This report describes concurrent photopolymer and VP system design to navigate this paradox with the unprecedented use of polymeric colloids (latexes) that effectively decouple the dependency of viscosity on molecular weight. Photocrosslinking of a continuous-phase scaffold, which surrounds the latex particles, combined with in situ computer-vision print parameter optimization, which compensates for light scattering, enables high-resolution VP of high molecular weight polymer latexes as particle-embedded green bodies. Thermal post-processing promotes coalescence of the dispersed particles throughout the scaffold, forming a semi-interpenetrating polymer network without loss in part resolution. Printing a styrene-butadiene rubber latex, a previously inaccessible elastomer composition for VP, exemplified this approach and yielded printed elastomers with precise geometry and tensile extensibilities exceeding 500%.

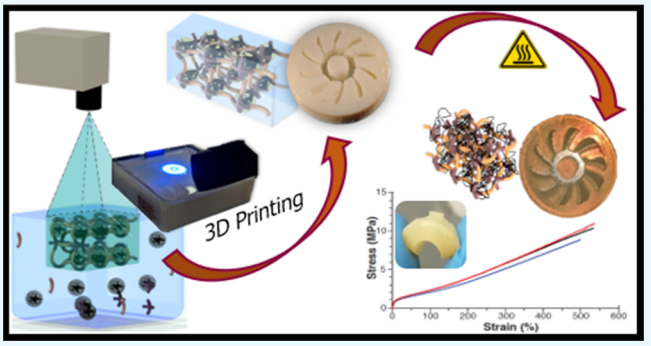

KEYWORDS: *vat photopolymerization, stereolithography, latex, elastomers, semi-interpenetrating polymer network, 3D printing, styrene-butadiene rubber, SBR*

1. INTRODUCTION

Vat photopolymerization (VP), also termed stereolithography, represents a versatile additive manufacturing (AM) platform, which enables the fabrication of precise and complex geometries that are unachievable through conventional polymer processing techniques. However, the printed objects typically comprise highly crosslinked, brittle polymeric networks, which severely restrict their utility as functional parts. VP conventionally delivers patterned UV light in a layer-by-layer fashion with free radical-initiated photocuring of liquid precursors. The resulting three-dimensional (3D) objects exhibit superior micron-scale resolution, isotropic mechanical properties, and surface finish compared to other AM platforms.[1,2] The typical maximum VP printable viscosity ($\lesssim$10 Pa·s) dictates the maximum molecular weight of the liquid precursors; the recoating process between the photocuring of each microscale layer is the primary determinant.[3] Successful VP printing demands that each layer provides sufficient modulus to maintain feature fidelity, and our preliminary efforts have identified a necessary storage modulus (typically in the 10^4−10^6 Pa range) to ensure feature fidelity in a printed object.[4−6] VP photocuring conventionally employs covalent crosslinking and high crosslink densities, which result in an imperfect network from low-molecular-weight precursors, leading to a suitable modulus but inferior mechanical performance (e.g., elasticity). Linear copolymerization of monomers in the VP printing environment, which potentially reduces crosslink density, fails to attain sufficient molecular weight in the printer due to atmospheric oxygen inhibition. Thus, current compositions in the literature do not achieve the prerequisite modulus without high concentrations of a crosslinking reagent.[7]

Elastomeric objects must reversibly deform to high elongations; however, the requisite high molecular weight between crosslink points (defined as M_c)[8] typically arises from low degrees of crosslinking of preformed, high molecular weight polymeric precursors (e.g., rubber vulcanization).[9] Thus, VP places additional functional constraints on polymeric precursors, demanding innovative synthetic strategies for increasing the M_c of printed networks. Current approaches

Received: November 4, 2019
Accepted: February 7, 2020
Published: February 7, 2020

https://dx.doi.org/10.1021/acsami.9b19986
ACS Appl. Mater. Interfaces 2020, 12, 10918−10928

involve the dissolution of high molecular weight polymers in organic solvents[4,10] or chain extension with reactive diluents.[5,6,11−13] However, both strategies do not adequately address M_c, and 3D structures of high molecular weight, olefin-derived, polymers (HDPE, PTFE, acrylics, and diene-based rubbers) are not achievable. Limitations of the earlier literature include solvent volatility, low polymer solubility in the diluent, and high solution viscosity for high molecular weight polymers. Thus, fundamental advances in both material and machine designs must concurrently address this paradox between VP polymer printability and final performance. Success at overcoming this challenge will broaden the versatility of polymer AM in modern manufacturing operations and create a vast library of unprecedented high molecular weight polymeric precursors.

Colloidal morphology effectively decouples the viscosity−molecular weight relationship for polymers with the sequestering of macromolecules into discrete nanoscale particles, which mitigates interchain entanglement. Polymeric colloids, often termed polymeric dispersions or latexes, typically comprise submicron polymer particles (termed the internal phase) that are uniformly dispersed in water (termed the continuous phase).[14,15] Polymeric colloids, including both natural (e.g., natural rubber latex)[16,17] and synthetic (e.g., acrylics and styrene-butadiene rubber latex), offer diverse compositions with high molecular weights, which are commonly on the order of 10^5−10^6 Da for emulsion-polymerized latexes.[18] For many decades, polymeric colloids have enabled facile processing of high molecular weight polymers at low viscosities for a variety of applications including, most notably, paints, coatings, and adhesives.[19−21] However, prior works in VP of latexes primarily focus on the printing of porous structures.[22−24] Thus, a design challenge remains for 3D coalescence of latex particles to access the mechanical properties of high molecular weight polymers in printed objects. Moreover, polymeric colloids scatter incident VP irradiation during printing, and intelligent energy distribution schemes for mitigating this scattering remain unexplored.

We report an unprecedented VP material and printing platform that employs common polymeric latexes as high molecular weight, low-viscosity precursors to address the VP printability-performance paradox. Photocrosslinking of water-soluble network precursors in the continuous phase forms a tunable scaffold that surrounds the latex particles, which yields a robust, freestanding green body object with suitable modulus for VP operations. We employ unprecedented computer-vision-based process parameter generation in the VP printer that compensates for light scattering by the colloid and enables light-based printing of complex shapes without UV absorbers. Subsequent dehydration of printed green bodies under mild conditions promotes 3D coalescence of the latex particles throughout the printed scaffold. This novel strategy forms a semi-interpenetrating polymer network (sIPN) and harnesses the mechanical properties of the dispersed, high molecular weight polymer without requiring extraordinary polymer thermal stability or disrupting the complex geometric features defined during the VP printing process. This leads to 3D-printed elastomers that establish a new benchmark for performance that approaches bulk elastomeric films.

2. RESULTS AND DISCUSSION

2.1. Synthetic Design of Photocurable Polymer Latexes. Figure 1 illustrates VP of photocurable polymeric

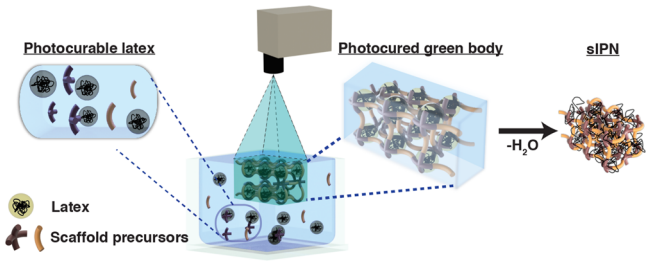

Figure 1. Vat photopolymerization printing and post-print processing of photocurable latex into semi-interpenetrating polymer networks (sIPN). Photocrosslinking of scaffold molecules in the continuous phase of latex entraps polymer particles into a solid green body. Drying of the green body enables the polymer within the particles to penetrate the scaffold and coalesce, harnessing the mechanical properties of the latex polymer.

latexes to print high molecular weight polymers. Facile addition of network precursors and photoinitiator to the continuous, aqueous phase of the latex enables photogeneration of the supporting scaffold. UV exposure during printing initiates photocrosslinking of these precursors to form a supporting scaffold around the latex particles, which yields a freestanding "green body" hydrogel embedded with high molecular weight latex particles. Subsequent drying and annealing of the green body enables the polymeric particles to diffuse and coalesce throughout the printed object. The resulting sIPN consists of two discrete components: (i) a photocrosslinked scaffold network, which serves to design the 3D shape of the object, and (ii) an entangled, high molecular weight latex polymer, which dictates mechanical performance of the final printed object. This strategy is suitable for any polymeric colloid; however, our initial focus on elastomers provides a convincing example of the importance of high molecular weight to attain high mechanical performance. Emulsion polymerization commonly affords styrene-butadiene rubber (SBR) latexes and represents a pervasive industrial elastomer otherwise unavailable for AM.

A suitable scaffold must meet three basic criteria: (i) scaffold monomers and photoinitiators must not disrupt the latex stability, (ii) scaffold monomers must rapidly photocure into a robust network capable of supporting colloidal particles in a 3D design with sufficient modulus for printing, and (iii) scaffold composition must enable both printability (curing kinetics and green body strength) and part performance (tensile strength and elasticity). Addressing each criterion is critical to enable robust green bodies, which maintain complex geometric features during printing and ensure desired performance upon particle coalescence and drying.

Illustrated in Figure 2, the combination of *N*-vinylpyrrolidinone (NVP) and poly(ethylene glycol) diacrylate (PEGDA) served as a suitable scaffold monomer and crosslinker, respectively, and this combination allowed VP-printed SBR latexes. Dynamic light scattering (DLS) (Figure 3C) confirmed that the scaffold monomers did not deleteriously influence the SBR particle size or particle size distribution. Photorheological measurements demonstrated the potential for efficient photocuring and desirable green body storage moduli as a function of UV light exposure (Figure S1). The plateau shear storage modulus (G_N^0) relates to the M_c of the photocrosslinked network[8] and ensures structural rigidity of the green body as a function of monomer composition, as shown in Figure 3F. G_N^0 increased significantly (8−200 kPa)

https://dx.doi.org/10.1021/acsami.9b19986
ACS Appl. Mater. Interfaces 2020, 12, 10918−10928

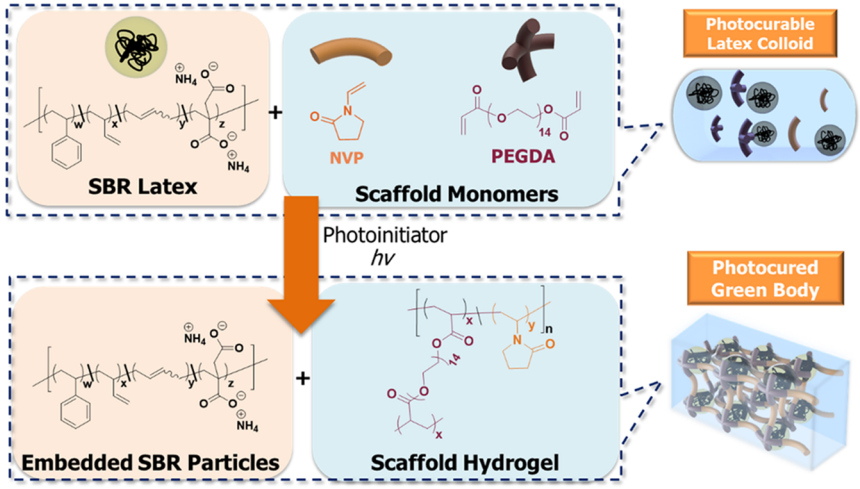

Figure 2. Continuous-phase photocrosslinking strategy to create photocurable latex. Incorporation of *N*-vinylpyrrolidinone (NVP) and poly(ethylene glycol) diacrylate (PEGDA) into continuous-phase enables photoactivated crosslinking and solidification of liquid latex.

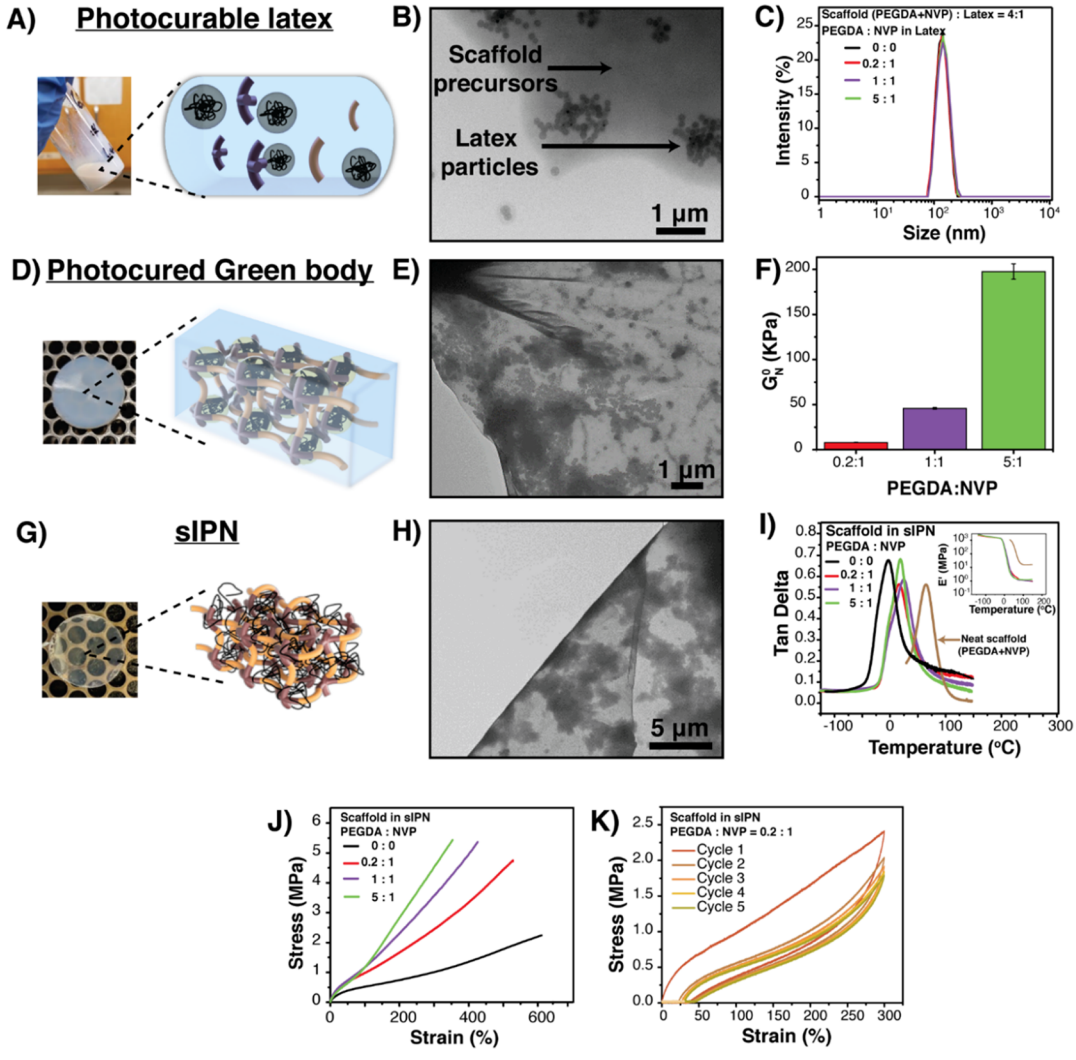

Figure 3. Investigation of photocurable latex to sIPN approach. (A) Photocurable latex. (D) Photocured green body. (G) Dried sIPN. (B) TEM of uncured, photocurable latex spin-casted on grid. Apparent aggregation of particles is artifact of sample preparation. (C) DLS confirms consistent particle size and distribution with and without scaffold monomers. (E) TEM of spin-casted photocured latex in the green body state. (F) Green body G_N^0 across scaffold compositions. (H) TEM of spin-casted photocured latex in the dried, IPN state. (I) DMA of sIPNs across scaffold composition. (J) Tensile performance of photocast and dried IPNs across scaffold compositions. (K) Cyclic loading to confirm elastic deformation and hysteresis (0.2:1 PEGDA:NVP).

https://dx.doi.org/10.1021/acsami.9b19986
ACS Appl. Mater. Interfaces 2020, 12, 10918−10928

with an increase in the concentration of the PEGDA crosslinker, that is, higher weight ratios of PEGDA:NVP. Tuning this ratio enabled optimization of both printing (higher G_N^0 for structural fidelity of green bodies) and final sIPN mechanical performance (lower G_N^0 for better tensile properties post drying). Considerations of colloidal stability restricted total scaffold loading (SBR:scaffold) to more narrow compositional ranges, and a 4:1 ratio (80 wt % SBR and 20 wt % scaffold) was deemed optimal for these studies.

Drying the photocured green bodies in vacuo changed the film appearance from opaque white to translucent (shown in Figure 3D,G), which was consistent with the loss of discrete, light-scattering nanoscale domains due to particle coalescence. Furthermore, their mechanical strength increased substantially from a soft, fragile green body hydrogel to ductile elastomers. Figure 3J illustrates the effect of scaffold composition on tensile behavior; in particular, sIPNs exhibit a higher ultimate stress and lower ultimate strain at higher scaffold crosslink densities (increased PEGDA:NVP). Previous literature examples of elastomer-based IPNs are similar as a function of both elastomer concentration and network crosslink density.[25−27] Moreover, a more highly crosslinked scaffold will presumably decrease the particles' ability to diffuse and coalesce, leading to less extensibility. sIPNs at the lowest scaffold crosslink density (lowest PEGDA:NVP wt ratio) achieved strains exceeding 500% and fully reversible deformation over five cycles at 300% strain (Figure 3K). It is important to note that crosslinked scaffold controls (without latex) were too brittle and prevented tensile specimen preparation, which further suggested that the scaffold serves as a structural template for the printed 3D shape; the interpenetrating, high molecular weight SBR polymer dominates the ultimate mechanical properties. Thus, VP of latexes enables printing of low-viscosity colloids that subsequently manifest mechanical performance of the high molecular weight polymers and, consequently, address the paradox of printability and performance for VP.

Transmission electron microscopy (TEM) revealed morphological transitions across the entire process from photocurable colloids to sIPNs. Spin-casted diluted latex samples (1 wt % solids) onto TEM grids enabled imaging of the latex particles. Photocuring and subsequent drying of these grids facilitated analysis of the green bodies and sIPNs, respectively. In the colloid precursor (Figure 3B), excellent contrast existed between the SBR particles and the scaffold monomers. TEM provided particle diameters that agreed well with DLS measurements in both the absence and presence of scaffold monomers, approximately 150 nm. The spin-coating process partially dries the samples, which presumably induces particle aggregation; DLS (Figure 3C) and wet-cell TEM (Figures S3 and S4) images confirm well-dispersed particles in the colloid precursor. Photocuring a spun-cast film on a TEM grid confirms a continuous scaffold film embedded with SBR particles (Figure 3E). Particles were only located within this film, suggesting that the network scaffold efficiently entraps the colloidal particles. After water removal in vacuo, the particles penetrated the scaffold and coalesced, and the loss of spherical shape and nanoscale phase separation supported this mechanism, as depicted in Figure 3H and Figure S2.

IPNs (containing two intertwined polymeric networks) and sIPNs (containing a single crosslinked network and non-crosslinked polymer) are widely recognized for their unique morphology and (thermo)mechanical properties.[28] Due to a high degree of network mixing, sIPNs commonly exhibit shifting of their component glass transition temperatures (T_g) to a single intermediate value, as predicted using the Fox relationship for random copolymers.[28,29] Dynamic mechanical analysis (DMA) (Figure 3I) shows a similar behavior for the all dried parts with single T_g's at approximately 16, 24, and 18 °C (as measured from DMA tan δ maxima) for the 5:1, 1:1, and 0.2:1 PEGDA:NVP, respectively. Each intermediate transition temperature favors the T_g of the major component, SBR (80 wt %), and occurs near the Fox prediction of 16 °C based on the T_g of the neat scaffold (1:1 PEGDA:NVP). It is important to note that these results also suggest an unprecedented methodology for preparing sIPNs with implications for membrane technologies beyond the scope of additive manufacturing.

2.2. Printing Light-Scattering Materials via Vat Photopolymerization. Our research demonstrates that photocurable latexes overcome the printability-mechanical performance paradox, enabling VP of high molecular weight polymers at a printable viscosity (<10 Pa·s); however, the existence of discrete colloidal particles introduces a new obstacle for VP. The colloidal particles in the photoreactive latex scatter the patterned UV light, which is incident on the liquid surface.[23] Light scattering (i) lowers the average intensity that the latex experiences, which lengthens cure times, and (ii) lowers the achievable printed feature resolution and the surface finish of the printed parts. To the best of our knowledge, a process-based approach to compensate for this scattering does not exist in the literature, and therefore others typically employ UV absorbing additives in colloidal printing examples.[24] These additives potentially disrupt colloidal stability and restrict versatility of a latex printing approach. Thus, a new printing method is required, in concert with latex design, to mitigate light-scattering effects. Our approach involves a computer-vision-based determination of printing parameters and enables precise fabrication of complex geometric features from polymer latexes.

Mitigation of light scattering in heterogeneous photopolymers requires (i) imaging of the scattered intensity distribution on the resin surface, (ii) prediction of resulting cured feature dimensions, and (iii) subsequent generation of corrected printing parameters (i.e., exposure time and gray scaling of the projected layer bitmap) to compensate for scattering effects and achieve target feature dimensions. Specifically, a machine-vision device (i.e., digital camera) images a projected UV test pattern and the scattered light around the projected pattern at the resin surface. A computer-vision algorithm then analyzes the captured image to extract the intensity distribution of a single projected pixel from the captured test pattern. In conjunction with part design specifications (layer bitmap pattern and thickness) and material curing parameters (depth of penetration, D_p, and critical energy, E_c), this computed single-pixel intensity profile quantifies scattering effects in the resin and enables the use of our previously described VP process model[30] to predict the cured feature dimensions for heterogeneous polymeric systems in VP. The approach employs an optimization scheme, and printing parameters are iteratively varied in the model to maximize the fit of the predicted cured feature dimensions with design specifications.

A digital camera captured the intensity map, $I_{camera}(X,Y)$, for a projected test pattern as a matrix with a relative intensity scale ranging from 0 to 255 (0 = lowest intensity level, 255 = highest intensity level). A computer-vision algorithm then

https://dx.doi.org/10.1021/acsami.9b19986
ACS Appl. Mater. Interfaces 2020, 12, 10918−10928

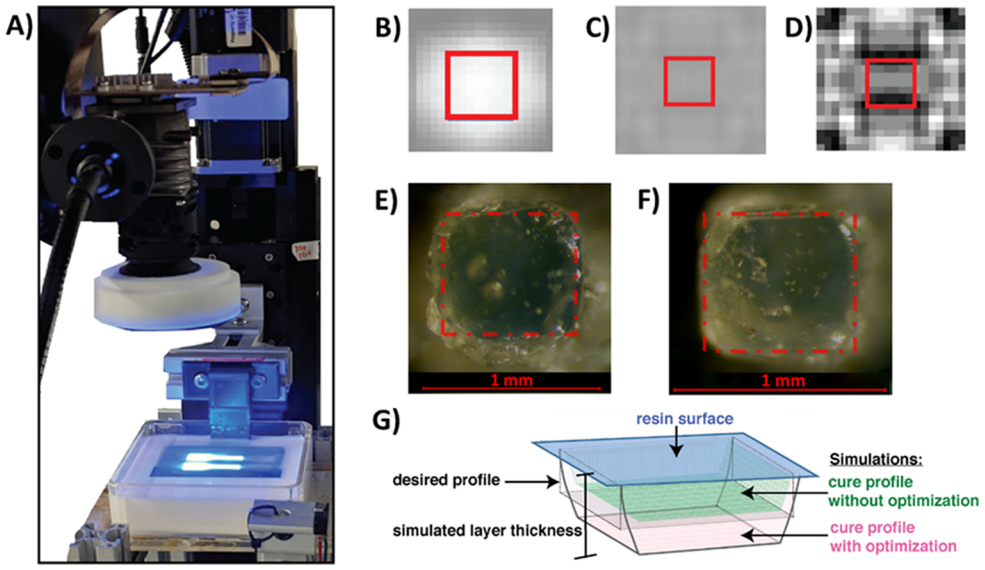

Figure 4. Vat photopolymerization of light-scattering latex. (A) Scanning mask projection vat photopolymerization (S-MPVP) enables fabrication of specimens with large footprint and high resolution. (B–D) In situ computer vision captures actual UV intensity distribution on the resin surface. (B) Clear resins scatter less UV light, which results in uniform gradation of intensity on the resin surface (white → gray), while (C) heterogeneous resins, such as the photocurable latex, scatter more UV light and lower the peak intensity distribution in the resin (gray throughout). (D) Normalization reveals non-uniform scattering inside the projection area. (E) Comparing the desired dimension (red box) with the square pillar printed without compensating for the *XY*-UV scatter highlights that the printed part exceeds design dimensions and has rounded edges with poor edge definition. (F) Compensating for *XY*-UV scatter through iterative optimization of projected intensity distribution results in the fabrication of pillars with improved dimensional accuracy and edge definition. (G) Modeling the energy distribution for specimens printed via a scanning process enables control of cure-through and dimensional accuracy by varying the scan speed and projection frame rate. The optimized printing parameters selected for this work are predicted to induce an *XY*-dimensional reduction of 8 μm at a cure depth of 100 μm. Truncating the cure depth by setting the layer thickness to 100 μm results in a cure profile that is similar to the desired profile.

extracted the intensity distribution of a preselected edge pixel ($I_{pix}(X,Y)$).[30] A thresholding condition (eq 1) enabled the computation of the extent and magnitude of spatial scatter (*XY* plane; i.e., resin surface) around the selected pixel. Inputting the captured single-pixel intensity distribution $I_{pix}(X,Y)$ into our previously described irradiance model[30] numerically reconstructed the overall intensity distribution of the projected test pattern ($I_{proj}(X,Y)$), as shown in eq 2. Normalizing and mapping the computed $I_{proj}(X,Y)$ with the mean actual projection intensity measured with a UV radiometer facilitated computation of the intensity levels in $I_{pix}(X,Y)$. Compared to homogeneous, clear systems, $I_{pix}(X,Y)$ for the latex elucidates extensive scattering and reduction in peak intensity, as evidenced by the low-intensity levels (gray) in the reconstructed image (Figure 3B,C). Scattering caused the projected intensity to spread to a radius of 58 μm (Figure 3C) from the center of the projected pixel, which is 28 μm more than homogeneous, clear resins. Normalizing $I_{pix}(X,Y)$ revealed non-homogeneous intensity distribution due to UV scattering by polymer particles in the projection area, as shown in Figure 4D.

$$I_{pix}(X, Y) = I_{camera}(X, Y), \text{ if } I_{camera}(X, Y) \geq I_{background} \quad (1)$$

where $I_{camera}(X,Y)$ and $I_{background}$ correspond to the intensity distribution captured by the camera and the threshold intensity value (when the resin is not irradiated with UV light), respectively.

$$I_{proj}(X, Y) = \sum I_{pix}(x, y) \times B_{i,j} \quad (2)$$

where *i*, *j* corresponds to the index of projected pixel in the bitmap image ($1 \leq i \leq 1920, 1 \leq j \leq 1080$), and $B_{i,j}$ is a discrete function that represents the state of the pixel in the bitmap pattern (i.e., $B_{i,j} = 1$ if the pixel at location "On" and $B_{i,j} = 0$ otherwise).

The previously developed energy and cure models[30] remained valid for the photocurable SBR latex due to adherence to the Jacobs equation[1] for target layer thicknesses under 700 μm (Figure S5). For the fabrication of small parts (<50 x 35 mm) with the standard mask projection vat photopolymerization apparatus, simulation of the energy profile and computation of cure width (l_w) for various exposure times (t) utilized the $I_{proj}(X,Y)$ input and predetermined curing parameters, that is, depth of penetration and critical energy, in the standard mask projection energy and cure models as shown in Eqs 3 and Eqs 4, respectively:

$$E_{proj}(X, Y, Z) = E_{proj}(X, Y) \times e^{-z/D_p}, \text{ for } 0 < z < Z \quad (3)$$

where $E_{proj}(X,Y) = I_{proj}(X,Y) \times t \ (0 < t < T)$

$$l_w(Z) = x_1 - x_2, \forall Z > 0 \quad (4)$$

where $x_1 = X$ when $E_{proj}(X,0, Z) = E_c$ as $X > 0$, and $x_2 = X$ when $E_{proj}(X,0, Z) = E_c$ as $X > x_1$.

Based on a predetermined exposure time for a desired layer thickness (via the Jacobs equation), a characterization specimen with square pillars was fabricated. The printed pillar (Figure 3E) and the simulations of the energy profiles for the Schwarz lattice (Figure S9) for the photocurable latex demonstrate poor edge definition and a disagreement between the projected cure width (l_w) and the design-specified width

https://dx.doi.org/10.1021/acsami.9b19986
ACS Appl. Mater. Interfaces 2020, 12, 10918–10928

(l_{wd}) due to light scattering. An optimization scheme (Scheme 1) corrected this inaccuracy, as demonstrated in Figure 3F, by iteratively varying the exposure time (t) and pixel gray-scaling ratio (p), which enabled both gross and fine control of cure width, respectively. As an illustrative example, the utilization of this optimization scheme to print a layer of the Schwarz primitive lattice from photocurable latex yielded an adjusted exposure time, gray-scaling ratio, and layer thickness of 8 s, 0.7, and 129 μm, respectively. Specimens were printed with a layer thickness of 100 μm to improve interlayer network formation.

Scheme 1. Optimization Scheme To Maximize Dimensional Conformance on the Resin Surface in the *XY* Plane for Static VP Systems (i.e., Line Width on the Resin Surface (l_w) = Design Line Width (l_{wd}))[a]

$$For: 0 < t < T \text{ and } 0 < p < 1$$

$$Solve: E_{proj}(X,Y,0)$$

$$where: I_{proj}(X,Y) = \sum_{i,j} p \times I_{pix}(X,Y) \times B_{i,j}, \forall (X,Y)$$

$$Subject\ to: |l_w - l_{wd}| \le 10^{-9}$$

[a]To enforce this condition, layer exposure time (t) and pixel gray-scale ratio (p), are iteratively incremented, and the resulting energy profile ($E_{proj}(X,Y,0)$) and the line width l_w are numerically computed. The optimization ends when $|l_w - l_{wd}|$ is less than the selected tolerance of 10^{-9}, and the resultant exposure time (t) and gray-scale ratio (p) are used for part fabrication.

The inverse relationship between the projection area and projection pixel size necessitated the utilization of our previously developed scanning mask projection VP mode (S-MPVP)[4,30] for fabrication of large parts (>50 × 35 mm) such as the tensile dog bone specimens (Figure S8). During S-MPVP, the projector scans across the resin surface (along the X axis) while projecting a movie (Figure 4A and Movie S1) of patterned UV light with a frame rate that is synchronized to the scanning velocity of the projector. In addition to increasing the printable XY scale, S-MPVP blends the intensity distributions of each pixel, and the synchronized movie ensures equal energy delivery (i.e., exposure time (t)) for each pixel location on the part surface, thus eliminating the need for the complex gray−scaling algorithms used in standard static mask projection VP systems. The total energy delivered ($E_{proj}(X,Y)$) to the resin is the cumulative spatial sum of the energy delivered during the scanning of each projected movie frame ($E_f(X_f,Y_f)$), as shown in eq 5. As before, computation of the energy profile inside the latex and the cured line width occurs according to eqs eqs 3 and eqs 4, respectively.

$$E_f(X_f, Y_f) = \frac{1}{v_s}\int_0^{X+r} I_f(x, Y)\mathrm{d}x \tag{5}$$

where r is the distance traveled by the projector, with velocity v_s, before the projector frame is updated. $v_s = \frac{r}{t}$, where t is the exposure time for a projected pixel. Thus, the frame rate of the movie (F_{rate}) then becomes $F_{rate} = \frac{1}{t}$.

$E_{proj}(X, Y) = E_{f1}(X_{f1}, Y_{f1}) + \cdots + E_{fn}(X_{fn}, Y_{fn})$, where X_{fn},Y_{fn} correspond to the local projection coordinate system for the nth frame, where $X_{fn} = X_{f(n-1)} + r$.

In an illustrative example, this approach simulated the fabrication of a 300 μm wide pillar, with r assumed to be equal to the pixel pitch (30 μm), for various exposure times. Like static VP scattering compensation, iterative variation of the exposure time (t) provided gross control to align the computed line width (l_w) on the resin surface with design specifications (l_{wd}), shown in Scheme 2. However, S-MPVP introduced the scan speed and frame rate as new print parameters, which, together with layer thickness, were subsequently computed using the optimized exposure time (Figure S6). The simulation with optimized and non-optimized parameters (Figure 4G) show that the line width with optimized parameters matches the designed line width and the cure profile resembles the desired cure profile when the cure depth is physically truncated by controlling the layer thickness. The optimized printing parameters in this work generated a cure profile with an XY dimension gradient of 8 μm for 100 μm cure depth and a cure through of 50 μm. The flowchart highlighting the process parameter generation for the S-MPVP process is show in Figure S6.

Scheme 2. Optimization Scheme To Maximize Dimensional Conformance on the Resin Surface in the *XY* Plane for Scanning VP Systems (i.e., Line Width on the Resin Surface (l_w) = Design Line Width (l_{wd}))[a]

$$For: 0 < t < T$$

$$Solve: E_{proj}(X,Y,0)$$

$$where: E_f(X_f,Y_f) = \frac{t}{r}\int_0^{X+r} I_f(x,Y)\,dx, \forall (X,Y)$$

$$Subject\ to: |l_w - l_{wd}| \le 10^{-9}$$

[a]Energy delivered to the resin in the scanning model is controlled by the exposure time per pixel (t). Hence, t is iteratively incremented, and the resulting intensity distribution for each frame ($I_f(x,Y)$) is computed. Then, the energy delivered to the resin surface ($E_{proj}(X,Y,0)$) and the line width l_w are numerically computed for each iteration of t. The optimization ends when $|l_w - l_{wd}|$ is less than the selected tolerance of 10^{-9}, and the resultant exposure time per pixel (t) is used to compute the scan speed and the frame rate used for part fabrication.

While the S-MPVP system coupled with a computer-vision-based process parameter generation enable fabrication of parts with high resolution, it was imperative that the UV-crosslinked green bodies demonstrated sufficient modulus to form self-supporting features, which withstand drag forces experienced during a recoating process. Furthermore, to achieve high-speed, high-resolution fabrication, the manifestation of green body strength must occur with a low UV exposure time (<10 s). G_N^0 serves as a metric for green body modulus, and irradiation time to modulus crossover ($G''/G' = 1$) gauges photocuring kinetics and aids in the determination of printability for the latex. A resin composition with 0.4:1 PEGDA:NVP was experimentally determined as an optimal composition for printing (G_N^0 = 30 kPa, crossover time of ∼1 s) while maintaining final sIPN ultimate strains above 500%. Printed green bodies, such as the lattice depicted in Figure 4A,B, demonstrate successful and accurate fabrication of positive (lattice struts) and negative features (designed voids) throughout the bulk of the green body. This demonstrates that high-resolution features are achievable

https://dx.doi.org/10.1021/acsami.9b19986
ACS Appl. Mater. Interfaces 2020, 12, 10918−10928

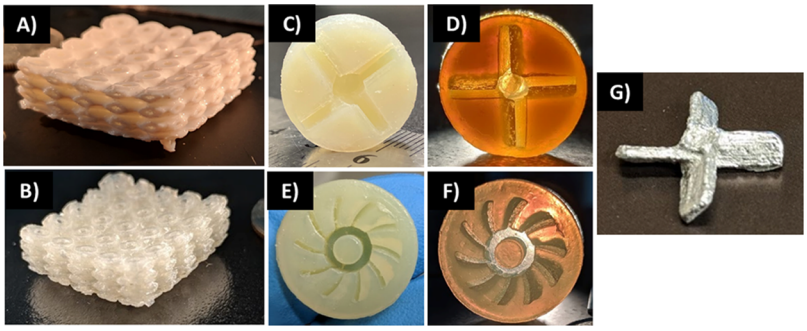

Figure 5. Evaluation of 3D objects printed from latex. (A–G) Images and performance of 3D-printed photocurable latex objects: 3D printed Schwarz lattice in (A) green body and (B) dried sIPN states, (C–F) printed elastomer molds, and (G) impellor casted from Field's metal alloy.

with light altered from light-scattering photoreactive polymeric colloids.

2.3. Evaluating Geometric Complexity and Elastic Performance of Printed Elastomers. Drying printed green bodies to yield elastic sIPNs results in the loss of a large volume fraction of water (~45 vol %), which is accompanied by a commensurate, isotropic volumetric shrinkage of approximately 40 vol % (dimensional shrinkage of 15.6%). Previous studies suggest the unique promise of isotropic shrinkage as a mechanism for increasing the resolution of printed structures.[4,31,32] Similar to our previous drying procedures,[4] slow isotropic drying on a porous substrate preserved the structural fidelity of the complex geometric features even for thicker objects (Figure 5). As shown in Figure S7, dry sIPN parts are optically clear along the direction of fabrication. This optical clarity confirms the absence of discrete interfaces between layers, which corroborates our previous work that attributes this feature to crosslinking between each layer.[4] Coalescence of particles both within and across layers further aids this process.

3D-printed tensile specimens (modified ASTM D-638 V) exhibit elongations over 500% with an average stress-at-break of 9.7 MPa (Figure S8), thereby representing the first example of a 3D-printed high-performance SBR elastomer. This approach successfully combined polymer performance with structural precision, enabling the fabrication of mechanically robust and reusable elastic molds, as shown in Figure 5. Specifically, we designed and printed a mold for an impeller with undercuts (i.e., profiles varying across $X-Y-Z$ planes; Figure S10A,B) to highlight an important application of printed elastomers: soft molding of complex geometries that cannot be directly extracted from hard molds. As a proof of concept, an impeller was casted in a 3D-printed SBR sIPN mold with Field's metal (a eutectic alloy of bismuth, indium, and tin) and successfully extracted from the soft mold without damaging either component (Figure 5G).

3. EXPERIMENTAL SECTION

3.1. Materials. Styrene-butadiene rubber (SBR) latex (Rovene 4176) was generously donated by Mallard Creek Polymers Inc. The latex has a solids content of 50 wt %, a particle diameter range of 120–170 nm, and a viscosity of 400 cps as measured by the manufacturer. The SBR copolymer was approximately 50/50 by weight styrene and butadiene with a low level of carboxylic acid monomer neutralized with ammonia to provide colloidal stability. The polymer contains a high insoluble (gel) content from the polymerization process due to intraparticle crosslinking during the polymerization process. 1-Vinyl-2-pyrrolidinone (NVP) and poly(ethylene glycol) (PEGDA 575, 575 g/mol), and diphenyl(2,4,6-trimethylbenzoyl)phosphine oxide (TPO) were purchased from Millipore Sigma and used as received.

3.2. Photocurable Latex Preparation. As a standard example (4:1 polymer:scaffold, 5:1 NVP:PEGDA), 50 mg of TPO photoinitiator was added to a 20 mL vial followed by the addition of 0.5 g NVP. The photoinitiator was fully dissolved via vortex mixing before addition of PEGDA and further mixing. The monomer/photoinitiator solution was then added via dropwise addition to 5 g of latex stirring rapidly in a separate 20 mL vial. The photocurable latex was then vortexed for 30 s to ensure complete mixing. For print-scale preparation, a similar method was used, employing a 1 L beaker and a mechanical stirrer during the monomer/photoinitiator addition to 400 g of latex.

3.3. Analytical Methods. Dynamic light scattering (DLS) measurements were conducted with a Malvern Zetasizer Nano, reporting intensity distributions. DLS samples were prepared with latex, which was diluted to 1 wt % solids with deionized water to minimize particle–particle interactions. Photorheology was performed on a TA Instruments DHR-2 equipped with a SmartSwap UV assembly with 20 mm aluminum upper plate, 20 mm quartz lower plate, and Omnicure S2000 high-pressure mercury light source (320–500 nm filter). UV intensity was measured with a Silverline radiometer and 20 mm sensor attachment for the quartz parallel plate. Data was gathered at a 500 μm gap, 0.2% strain, and 1 Hz. UV radiation was applied at an intensity 200 mW/cm^2 for 150 s after a 30 s delay. The rheometer was set to maintain 0 N axial force within a ± 1 N tolerance through slight adjustments in gap size. Samples were run under air without purge of inert gas. All samples were run in triplicate to ensure consistency and reproducibility of this technique. Plateau storage moduli values were calculated from the last 20 s of the G' curve; moduli crossover (G'/G'') values were determined using the dedicated feature in TA Instruments TRIOS software. Gel fractions were determined as the difference in dry weight before and after extraction and averaged over three replicates. Density measurements were conducted with a specific gravity kit and balance according to a previously reported procedure.[16] Dynamic mechanical analysis (DMA) was performed on a TA Instruments Q800 Dynamic Mechanical Analyzer in tension mode at 1 Hz frequency, 0.2% strain amplitude, and a heating rate of 3 °C/min −140 to 150 °C. Tensile experiments were performed on an Instron 5500R tensile tester at a strain rate of 5 mm/min at 23 °C. Measurements of engineering stress at 100% strain in addition to engineering stress and strain at break are reported. Hysteresis experiments were performed on the same instrument from 0–300% strain at a strain rate of 20% strain/min.

3.4. Preparation of TEM Samples. Transmission electron microscopy (TEM) was performed in the dried state on spin-coated TEM grids (Formvar/Carbon 200 mesh, copper) and in a liquid state via BioMatek k-kits with a 200 nm channel height purchased through Ted Pella. Imaging was performed with both a Philips EM420 (120 kV acceleration voltage) and a JEOL 2100 (200 kV acceleration voltage) for the dry and liquid-state samples, respectively.

3.4.1. Spin-Casted and Photocured TEM Grids. Photocurable latex (4:1 polymer:scaffold, 5:1 NVP:PEGDA) was prepared as described

https://dx.doi.org/10.1021/acsami.9b19986
ACS Appl. Mater. Interfaces 2020, 12, 10918–10928

above using 1 wt % diluted latex in lieu of 50 wt % to aid imaging. Pure latex (without monomer and photoinitiator) at 1 wt % dilution was also prepared for comparison. Seventy microliters of each latex sample was then applied to the surface of a TEM grid and spin-coated at 4000 rpm for 20 s. For photocured samples (green body and IPN state), UV irradiation was applied via an Omnicure S2000 (details above) at 10% shutter for 5 s. IPN state samples were placed in a vacuum oven at 65 °C for 12 h. All other samples were mounted onto a glass slide and placed into a sealed centrifuge tube with water-saturated Kimwipes to minimize drying prior to imaging. TEM imaging occurred promptly after sample preparation. The wet samples were placed directly into the TEM sample load lock to rapidly dry immediately before insertion into the instrument and imaging. The dried (IPN state) sample was imaged after directly after removal from a vacuum oven.

3.4.2. Liquid-Cell (k-kit) TEM (Wet-State). Photocurable latex (4:1 polymer:scaffold, 5:1 NVP:PEGDA) was prepared as described above using 1 wt % diluted latex in lieu of 50 wt % to aid imaging and a neat 1 wt % without added monomer and photoinitiator for comparison. Each sample was loaded into the k-kit according to a modified version of the procedure provided with the k-kit toolkit and employing a stereoscope for visualization of the process. Latex (0.2 μL) was placed on the sample loading stage. The k-kit channel ends were opened via removing the sealing tips at each end, and then one end of the channel was dipped into the sample droplet, ensuring contact via stereoscope observation. The ends of the k-kit body were cleaned using polypropylene swabs followed by sealing of each end with Hysol 1C high vacuum sealant. The k-kit was allowed to sit for 1 h at atmospheric temperature and pressure to allow hardening of the sealant before mounting into the provided copper grid holder with the supplied epoxy. The k-kit was then placed in a vacuum oven at 15 mmHg and room temperature to accelerate curing of the sealant and mounting epoxy. Finally, the sample was covered in aluminum foil and stored in a cool, dark place overnight to allow full curing of the sealant.

3.5. Preparation of DMA Samples. Green body discs cured via photorheology as described previously. The green body discs were then dried in the vacuum oven at 65 °C for 12 h, extracted in acetone for 12 h, and subsequently dried in vacuo at room temperature for an additional 12 h. Rectangular specimens were cut from the IPN disc films and analyzed directly.

3.6. Preparation of Dogbones from Photocast Films for Tensile Analysis. Photocurable latex was prepared as described above. Three grams of each sample was placed into a glass Petri dish (9 cm diameter) and irradiated for 30 s on each side with a belt-fed photocuring system (LC-6B) from Fusion UV Systems Inc. equipped with a 100 W bulb. The films were subsequently dried in vacuum oven at 65 °C for 12 h to allow drying and particle coalescence. The IPN films were then removed from the Petri dish and extracted in acetone for 12 h before another drying step in a vacuum oven at room temperature for 12 h to remove acetone. Dogbones were then cut from the dried and extracted films using a Pioneer-Dietecs ASTM D-638-V die and analyzed directly.

3.7. Vat Photopolymerization of Latex. *3.7.1. Scanning Mask Projection Vat Photopolymerization Apparatus (S-MPVP).* A custom S-MPVP apparatus was used for specimen fabrication.[30] The apparatus comprises a high-resolution projector with 1080p Texas Instruments DMD (0.65″). The projector is illuminated by Dymax Bluewave 75 spot-cure lamp with a broad-spectrum emission in the range of 300−500 nm. The intensity on the projection plane, measured with a 365 nm radiometer (xx name), is 2.4 mW/cm^2. Using imaging and conditioning optics (DLIinnovations-DLP6500), the projection area and projected pixel size on the focal plane were measured to be 61 × 34 mm and 31 μm, respectively. The projector is fixed on cross-mounted $X-Y$ linear stages (ZABER: A-LST0500A-E01) to enable continuous scanning in the $X-Y$ plane. A build stage, additively manufactured using filament extrusion of ULTEM 9085, is mounted to a high-resolution Z-stage (ZABER: A-LST0250A-E01). A glass slide (Corning 294775X50) was mounted to the top surface of the build platform to ensure a smooth build surface and good adhesion with the printed part. A custom glass vat (150 × 150 × 40 mm) was manufactured for containing the photocurable latex. A recoating blade, mounted to a custom linear actuator, was directly mounted to the $X-Y$ gantry, enabling the control over recoating speed and recoating depth. The mechatronic elements and the projection were controlled using a custom LABVIEW program.[30]

The scanning mask projection apparatus was used in this work because it enables the fabrication of large area parts with high resolution through the use of the unique scanning process. Instead of projecting a static frame on the resin surface, the S-MPVP system projects a movie and scans across the resin surface simultaneously. During the fabrication process, a bitmap corresponding to the layer to be printed is sliced into smaller projection rows. Each row is then split into multiple static frames such that when they are played as a movie, the entire row is projected without loss of information. The speed at which the movie is played is related to the scan speed through the S-MPVP model. Through the use of a custom rendering program, the movie is created and played real-time while the projector is scanning across the resin surface. This process is repeated for all the scanning rows and all layers if the part to be fabricated. The synchronization of the movie and the scanning process are carefully monitored to ensure consistent part fabrication.

3.7.2. Working Curve Generation. Thirty milliliters of photocurable latex was transferred into a glass Petri dish and placed in the focal plane of the projector. A test feature (20 × 20 pix) was projected on the resin surface with exposure times of 5, 6, 7, 8, 10, 11, 12, and 18 s. The resulting cured specimens were rinsed with water and UV post-cured (Melodysusie 36 W, 365 nm) for 10 min each side. The thickness of the specimens was plotted against exposure to generate the working curve to compute the values for critical energy and depth of penetration (resin curing parameters) (Figure S5).[1]

3.7.3. Printing Parameter Generation with the S-MPVP Model. The intensity distribution, resulting from the projection of a 1 pixel wide line on the resin surface, was captured with an embedded digital camera (Logitech C920) and processed using a custom computer vision (MATLAB) program. Using a depth of penetration (D_p) and critical energy (E_c), computed via a working curve, of 206 μm and 74 mJ/cm^2, respectively, the S-MPVP model was applied to the test specimen.[30]

The reference energy distribution required to fabricate an accurate test specimen was numerically determined by setting all the energy levels equal to the resin's E_c. Then, the bitmap pattern corresponding to a layer to be fabricated was fed into the irradiance model (eq 2), and the actual intensity distribution on the resin surface was computed. Using an algorithm to iteratively select the exposure time and projection intensity, the cured specimen dimensions were simulated with the S-MPVP model, and multiple energy distributions were generated. The simulated cure dimensions were then compared against the desired specimen dimension. The combination of exposure time and intensity that resulted in fabrication of feature with an error of <10 μm was selected for specimen fabrication. The flowchart for the process parameter optimization is shown in Figure S6.

For fabrication of specimens in the static mode, the optimization algorithm was modified as per Scheme 1. Through iterative selection of exposure time and gray-scaling ratio, the cured specimen dimensions were simulated with the S-MPVP model. The combination of process parameters that resulted in the fabrication of features with errors of <10 μm was selected for specimen fabrication.

3.7.4. Specimen Fabrication via Static MPVP. Autodesk Netfabb was used to slice the STL file of the Schwarz lattice (pore size of 5 mm) and the impellor molds into 100 μm layers. The layers were then converted into bitmap images with a resolution of 801 DPI. Photocurable latex was transferred into the resin vat, and the build platform was lowered 100 μm (layer thickness) into the resin. The projector, while remaining stationary above the build platform, projected bitmap patterns corresponding to each layer for an exposure time of 8 s. The first layer was exposed three times to ensure good adhesion with the glass slide. The build platform was then lowered

https://dx.doi.org/10.1021/acsami.9b19986
ACS Appl. Mater. Interfaces 2020, 12, 10918−10928

into the resin to agitate the latex and prevent evaporation of water. After accounting for the layer thickness, the build platform was raised to the appropriate height for recoating. A recoating blade traversed across the printed tensile specimen to enforce deposition of a uniform layer of uncured resin. The recoating speed was controlled to 5 mm/s to prevent dislodging of printed specimen. The projection and recoating cycles were repeated until complete fabrication of the part. Printed green bodies were removed from the build platform and cleaned thoroughly with water to remove uncured resin. Cleaned green bodies were UV-post-cured for 10 min (each side).

3.7.5. Specimen Fabrication via Scanning Mask Projection Vat Photopolymerization (S-MPVP). Autodesk Netfabb was used to slice the STL file of the tensile specimens (modified ASTM-638 V) into 100 μm layers. The layers were then converted into bitmap images with a resolution of 801 DPI. Photocurable latex was transferred into the resin vat, and the build platform was lowered 100 μm (layer thickness) into the resin. The projector scanned across the resin surface with a scan speed of 4.286 mm/s while simultaneously projecting the generated bitmap layers as a movie with a frame rate of 135 frames/s. The first layer was exposed three consecutive times to ensure good adhesion with the glass slide. The build platform was then lowered into the resin to agitate the latex and prevent evaporation of water. After accounting for the layer thickness, the build platform was raised to the appropriate height for recoating. A recoating blade traversed across the printed tensile specimen to enforce deposition of a uniform layer of uncured resin. The recoating speed was controlled to 5 mm/s to prevent dislodging of the printed specimen. The projection and recoating cycles were repeated until complete fabrication of the part. Printed green bodies were removed from the build platform and cleaned thoroughly with water to remove uncured resin. Cleaned green bodies were UV-post-cured for 10 min (each side).

3.7.6. Post-Processing of 3D Printed Objects. Post-cured specimens were transferred onto Teflon sheets and placed in a vacuum oven preheated to 45 °C. The specimens were placed under vacuum (3 in. Hg) for 48 h. The pressure inside the vacuum chamber was slowly equilibrated over 10 min, and the dried parts were removed for imaging and mechanical testing.

4. CONCLUSIONS

We report concurrent polymer and machine design to address the vat photopolymerization (VP) printability-mechanical performance paradox with photoreactive polymeric colloids (latex); we report the first-ever printed styrene-butadiene rubber (SBR) elastomer. The introduction of tunable photoreactivity into polymer latex and computer-vision-based process parameter generation enabled VP printing of polymeric colloids to yield mechanically strong and geometrically complex 3D geometries. An unprecedented strategy for sIPN formation manifests the mechanical properties of the dispersed polymeric particles upon 3D coalescence throughout the printed object without disrupting feature fidelity. This work expands the opportunities for VP printing of elastomers with intricate features that exhibit extensibilities above 500%, nearly 200% above the leading commercial VP elastomers.[33] The tunability and modularity of this approach, when combined with diverse scaffold and polymeric particle compositions, suggests versatility beyond SBR latexes and elastomers.

■ ASSOCIATED CONTENT

Supporting Information

The Supporting Information is available free of charge at https://pubs.acs.org/doi/10.1021/acsami.9b19986.

(Figures S1−S10) Photocuring of PEGDA and NVP in the continuous phase of SBR latex yielding hydrogel embedded with SBR particles, drying of photocured green bodies yielding translucent sIPN networks, TEM images of photocured latex green body in the wet state (k-kit) showing well-dispersed particles throughout the curing process, TEM images of photocured latex in the dried state (k-kit) showing well-dispersed particles with increased radius due to penetration with scaffold, working curve of the 0.25:1 PEGDA:NVP latex composition, the flowchart highlighting the method to determine the process parameters for printing with the S-MPVP system, VP-printed cubes from the 0.4:1 PEGDA:NVP latex composition for shrinkage analysis, tensile analysis of VP-printed tensile specimens (0.4:1 PEGDA:NVP), single-pixel intensity distribution captured via computer vision, and CAD models used for fabricating the specimens and (Table S1) (thermo)-mechanical data for sIPNs and neat SBR from latex (PDF)

(Movie S1) Scanning mask projection vat photopolymerization (S-MPVP) printing photocurable latex into dog-bone specimens (MP4)

(Movie S2) Physical manipulation of printed lattice from photocurable latex (0.4:1 PEGDA:NVP scaffold composition) (MP4)

(Movie S3) Physical manipulation of printed mold from 0.4:1 PEGDA:NVP to demonstrate mold's ability to reversibly deform for part extraction (MP4)

■ AUTHOR INFORMATION

Corresponding Author

Timothy E. Long − *Macromolecules Innovation Institute and Department of Chemistry, Virginia Tech, Blacksburg, Virginia 24061, United States;* orcid.org/0000-0001-9515-5491; Email: telong@vt.edu

Authors

Philip J. Scott − *Macromolecules Innovation Institute and Department of Chemistry, Virginia Tech, Blacksburg, Virginia 24061, United States;* orcid.org/0000-0002-4219-6000

Viswanath Meenakshisundaram − *Macromolecules Innovation Institute and Department of Mechanical Engineering, Virginia Tech, Blacksburg, Virginia 24061, United States;* orcid.org/0000-0003-3589-6030

Maruti Hegde − *Macromolecules Innovation Institute and Department of Chemistry, Virginia Tech, Blacksburg, Virginia 24061, United States; Department of Applied Physical Sciences, University of North Carolina, Chapel Hill, North Carolina 27514, United States*

Christopher R. Kasprzak − *Macromolecules Innovation Institute and Department of Chemistry, Virginia Tech, Blacksburg, Virginia 24061, United States*

Christopher R. Winkler − *Nanoscale Characterization and Fabrication Laboratory (NCFL), Virginia Tech, Blacksburg, Virginia 24061, United States;* orcid.org/0000-0002-5874-0787

Keyton D. Feller − *Macromolecules Innovation Institute and Department of Mechanical Engineering, Virginia Tech, Blacksburg, Virginia 24061, United States;* orcid.org/0000-0001-7972-149X

Christopher B. Williams − *Macromolecules Innovation Institute and Department of Mechanical Engineering, Virginia Tech, Blacksburg, Virginia 24061, United States*

https://dx.doi.org/10.1021/acsami.9b19986
ACS Appl. Mater. Interfaces 2020, 12, 10918−10928

Complete contact information is available at:
https://pubs.acs.org/10.1021/acsami.9b19986

Author Contributions

#P.J.S. and V.M. contributed equally to this work as co-first authors. The manuscript was written through contributions of all authors. All authors have given approval to the final version of the manuscript. P.J.S., M.H., and T.E.L. developed the concept for photocurable latex synthesis and sIPN formation. P.J.S. and C.R.K. performed synthesis and material characterization. C.R.K. developed the optimal scaffold composition for printing. P.J.S., C.R.K., and K.D.F. performed characterization of photocuring and (thermo)mechanical properties. V.M. and C.B.W. designed and built the VP printer used for this work and invented the printing process model and print parameter generation scheme for static and scanning VP systems that enabled printing heterogeneous materials with light. C.R.W. and P.J.S. designed and performed all TEM studies. P.J.S., V.M., C.B.W, and T.E.L. wrote the paper with major contributions from M.H. for critical revision and figure design. T.E.L. and C.B.W. secured funding for this project.

Funding

This work was partially funded by the Michelin North America, Inc. and currently funded by the National Science Foundation (NSF) GOALI grant in partnership with Michelin (CMMI − 1762712).

Notes

The authors declare the following competing financial interest(s): This strategy for VP printing latex is the subject of a provisional patent filed by the authors (U.S. Provisional Patent Application No.: 62/823,478).

■ ACKNOWLEDGMENTS

The authors acknowledge Dan Derbyshire and Mallard Creek Polymers for their generous donation of SBR latex and details on their materials. The authors also thank Prof. Joserra Leiza and Dr. Miren Aguirre at the University of the Basque Country for insightful discussions and their expertise in the synthesis and characterization of polymer latex. We acknowledge Chris Chen and Bio Ma-Tek for supplying k-kits for liquid-state TEM analysis and their expertise during implementation of these devices. The authors thank our collaborators at the Michelin North America, Inc.: Donald Lorey, Elizabeth Hotaling, Greg Gossweiler, Clay Bohn, and Michael Andrews for their expertise in diene elastomers.

■ REFERENCES

(1) Jacobs, P. F. *Rapid Prototyping & Manufacturing: Fundamentals of Stereolithography*; Society of Manufacturing Engineers: Dearborn, MI, USA, 1992.
(2) Gibson, I.; Rosen, D.; Stucker, B. *Additive Manufacturing Technologies: 3D Printing, Rapid Prototyping, and Direct Digital Manufacturing*; Springer-Verlag New York: New York, NY, 2015.
(3) Halloran, J. W. Ceramic Stereolithography: Additive Manufacturing for Ceramics by Photopolymerization. *Annu. Rev. Mater. Res.* **2016**, *46*, 19.
(4) Hegde, M.; Meenakshisundaram, V.; Chartrain, N.; Sekhar, S.; Tafti, D.; Williams, C. B.; Long, T. E. 3D Printing All-Aromatic Polyimides using Mask-Projection Stereolithography: Processing the Nonprocessable. *Adv. Mater.* **2017**, *29*, 1701240.
(5) Scott, P. J.; Meenakshisundaram, V.; Chartrain, N. A.; Sirrine, J. M.; Williams, C. B.; Long, T. E. Additive Manufacturing of Hydrocarbon Elastomers via Simultaneous Chain Extension and Cross-linking of Hydrogenated Polybutadiene. *ACS Appl. Polym. Mater.* **2019**, *1*, 684.
(6) Sirrine, J. M.; Meenakshisundaram, V.; Moon, N. G.; Scott, P. J.; Mondschein, R. J.; Weiseman, T. F.; Williams, C. B.; Long, T. E. Functional Siloxanes with Photo-activated, Simultaneous Chain Extension and Crosslinking for Lithography-Based 3D printing. *Polymer* **2018**, *152*, 25.
(7) Wilts, E. M.; Pekkanen, A. M.; White, B. T.; Meenakshisundaram, V.; Aduba, D. C., Jr.; Williams, C. B.; Long, T. E. Vat Photopolymerization of Charged Monomers: 3D printing with Supramolecular Interactions. *Polym. Chem.* **2019**, *10*, 1442.
(8) Rubinstein, M.; Colby, R. H. *Polymer Physics*; Oxford University Press: New York, NY, USA, 2003.
(9) Akiba, M.; Hashim, A. S. Vulcanization and Crosslinking in Elastomers. *Prog. Polym. Sci.* **1997**, *22*, 475.
(10) van Bochove, B.; Schüller-Ravoo, S.; Grijpma, D. W. Photo-Crosslinked Elastomeric Bimodal Poly(trimethylene carbonate) Networks. *Macromol. Mater. Eng.* **2019**, *304*, 1800623.
(11) Thrasher, C. J.; Schwartz, J. J.; Boydston, A. J. Modular Elastomer Photoresins for Digital Light Processing Additive Manufacturing. *ACS Appl. Mater. Interfaces* **2017**, *9*, 39708.
(12) Patel, D. K.; Sakhaei, A. H.; Layani, M.; Zhang, B.; Ge, Q.; Magdassi, S. Highly Stretchable and UV Curable Elastomers for Digital Light Processing Based 3D Printing. *Adv. Mater.* **2017**, *29*, 1606000.
(13) Rolland, J. P.; Chen, K.; Poelma, J.; Goodrich, J.; Pinschmidt, R.; DeSimone, J. M.; Robeson, L. M. Polyurethane Resins Having Multiple Mechanisms of Hardening for Use in Producing Three-Dimensional Objects. US 9,453,142 B2, 2016.
(14) Berg, J. C. *An Introduction to Interfaces and Colloids: The Bridge to Nanoscience*; World Scientific Publishing Company: Singapore, 2009.
(15) Israelachvili, J. N. *Intermolecular and Surface Forces*; Academic Press: Cambridge, MA, USA, 2011.
(16) Greve, H. H. Rubber 2. Natural. In *Ullmann's Encyclopedia of Industrial Chemistry*; Wiley-VCH: Weinheim, Germany, 2000, Ch. 2.
(17) Verhaar, G. Natural Latex as a Colloidal System. *Rubber Chem. Technol.* **1959**, *32*, 1627.
(18) Asua, J. M. Emulsion Polymerization: From Fundamental Mechanisms to Process Developments. *J. Polym. Sci., Part A: Polym. Chem.* **2004**, *42*, 1025.
(19) Shields, J. *Adhesives handbook*; Elsevier: New York, NY, USA, 2013.
(20) Takemoto, S. G.; Morrison, O. J. Pressure-Sensitive Adhesives Based on Carboxylated SBR Emulsion. US 4,189,419 A, 1980.
(21) Ma, Y.; Davis, H. T.; Scriven, L. E. Microstructure Development in Drying Latex Coatings. *Prog. Org. Coat.* **2005**, *52*, 46.
(22) Hsiao, L. C.; Badruddoza, A. Z. M.; Cheng, L. C.; Doyle, P. S. 3D Printing of Self-Assembling Thermoresponsive Nanoemulsions into Hierarchical Mesostructured Hydrogels. *Soft Matter* **2017**, *13*, 921.
(23) Zhu, C.; Pascall, A. J.; Dudukovic, N.; Worsley, M. A.; Kuntz, J. D.; Duoss, E. B.; Spadaccini, C. M. Colloidal Materials for 3D Printing. *Annu. Rev. Chem. Biomol. Eng.* **2019**, *10*, 17.
(24) Zhang, Y.; Yin, M.; Xia, O.; Zhang, A. P.; Tam, H. N. Optical 3D μ-printing of Polytetrafluoroethylene (PTFE) Microstructures. In *2018 IEEE Micro Electro Mechanical Systems (MEMS)*; IEEE: Piscataway, NJ, USA, 2018.
(25) Morin, A.; Djomo, H.; Meyer, G. C. Polyurethane-Poly(methyl methacrylate) Interpenetrating Polymer Networks: Some Mechanical Properties. *Polym. Eng. Sci.* **1983**, *23*, 394.
(26) Akay, M.; Rollins, S. N. Polyurethane-poly(methyl methacrylate) Interpenetrating Polymer Networks. *Polymer* **1993**, *34*, 1865.
(27) Jajam, K. C.; Bird, S. A.; Auad, M. L.; Tippur, H. V. Tensile, Fracture and Impact Behavior of Transparent Interpenetrating Polymer Networks with Polyurethane-Poly(methyl methacrylate). *Polym. Test.* **2013**, *32*, 889.

(28) Klempner, D.; Sperling, L. H.; Utracki, L. A. *Interpenetrating Polymer Networks*; American Chemical Society: Washington, DC, USA, 1994.
(29) Donatelli, A. A.; Sperling, L. H.; Thomas, D. A. Interpenetrating Polymer Networks Based on SBR/PS. 1. Control of Morphology by Level of Cross-linking. *Macromolecules* **1976**, *9*, 671.
(30) Meenakshisundaram, V.; Sturm, L. D.; Williams, C. B. Modeling A Scanning-Mask Projection Vat Photopolymerization System for Multiscale Additive Manufacturing. *J. Mater. Process. Technol.* **2020**, *279*, 116546.
(31) Oran, D.; Rodriques, S. G.; Gao, R.; Asano, S.; Skylar-Scott, M. A.; Chen, F.; Tillberg, P. W.; Marblestone, A. H.; Boyden, E. S. 3D Nanofabrication by Volumetric Deposition and Controlled Shrinkage of Patterned Scaffolds. *Science* **2018**, *362*, 1281.
(32) Long, T. E.; Williams, C. B. Printing Nanomaterials in Shrinking Gels. *Science* **2018**, *362*, 1244.
(33) Rolland, J. P. Functional Materials for 3D Manufacturing using Carbon's CLIP Technology. *J. Photopolym. Sci. Technol.* **2016**, *29*, 451.

https://dx.doi.org/10.1021/acsami.9b19986
ACS Appl. Mater. Interfaces 2020, 12, 10918−10928